



Article

Manipulable Electronic and Optical Properties of Two-Dimensional MoTe/MoGe₂N₄ van der Waals Heterostructures

Jiali Wang¹, Xiuwen Zhao¹, Guichao Hu¹, Junfeng Ren^{1,2,*} and Xiaobo Yuan^{1,*}

¹ School of Physics and Electronics, Shandong Normal University, Jinan 250358, China; 2020020533@stu.sdnu.edu.cn (J.W.); xwzhao@sdnu.edu.cn (X.Z.); hgc@sdnu.edu.cn (G.H.)

² Shandong Provincial Engineering and Technical Center of Light Manipulations & Institute of Materials and Clean Energy, Shandong Normal University, Jinan 250358, China

* Correspondence: renjf@sdnu.edu.cn (J.R.); yxb@sdnu.edu.cn (X.Y.)

Abstract: van der Waals heterostructures (vdWHs) can exhibit novel physical properties and a wide range of applications compared with monolayer two-dimensional (2D) materials. In this work, we investigate the electronic and optical properties of MoTe/MoGe₂N₄ vdWH under two different configurations using the VASP software package based on density functional theory. The results show that Te₄-MoTe/MoGe₂N₄ vdWH is a semimetal, while S₄-MoTe/MoGe₂N₄ vdWH is a direct band gap semiconductor. Compared with the two monolayers, the absorption coefficient of MoTe/MoGe₂N₄ vdWH increases significantly. In addition, the electronic structure and the absorption coefficient can be manipulated by applying biaxial strains and changing interlayer distances. These studies show that MoTe/MoGe₂N₄ vdWH is an excellent candidate for high-performance optoelectronic devices.



Citation: Wang, J.; Zhao, X.; Hu, G.; Ren, J.; Yuan, X. Manipulable Electronic and Optical Properties of Two-Dimensional MoTe/MoGe₂N₄ van der Waals Heterostructures. *Nanomaterials* **2021**, *11*, 3338. <https://doi.org/10.3390/nano11123338>

Academic Editor: Maurizio Passacantando

Received: 5 November 2021
Accepted: 6 December 2021
Published: 8 December 2021

Publisher's Note: MDPI stays neutral with regard to jurisdictional claims in published maps and institutional affiliations.



Copyright: © 2021 by the authors. Licensee MDPI, Basel, Switzerland. This article is an open access article distributed under the terms and conditions of the Creative Commons Attribution (CC BY) license (<https://creativecommons.org/licenses/by/4.0/>).

Keywords: van der Waals heterostructure; electronic structure; optical absorption

1. Introduction

Two-dimensional (2D) materials with different physical properties have been discovered in the last few decades, such as graphene, hexagonal boron nitride (h-BN), layered metal oxides, and transition metal dichalcogenides (TMDs) [1–5]. As one of the research hotspots in 2D materials, TMD materials are promising in nanoelectronics, optoelectronics, and photocatalytic devices [6–10]. TMD monolayers can be expressed as MX₂, in which M represents the transition metal atom and X refers to the halogen atom. The lattice structure of TMDs is similar to a “sandwich” structure. The transition metal atom M is sandwiched between two layers of halogen atom X, which are connected by chemical bonds. One layer of the halogen atom X in MX₂ can be replaced by another halogen atom Y, which can form a non-centrosymmetric structure and is referred to as Janus materials with the chemical formula Janus MXY [11,12]. Janus MXY have many unique physical properties that distinguish them from conventional 2D materials, including strong in-plane piezoelectric polarization [13], valley splitting [14], Rashba spin splitting [15,16], and good catalytic properties [17]. In recent years, people have conducted a lot of research on Janus MXY for M = Mo, W and X, Y = S, Se, Te, etc. As a typical representative of Janus MXY material, the Janus MoS₂ monolayer has been successfully manufactured by replacing the Se atom at the top of the MoSe₂ monolayer with the S atom, which provides experimental guidance for the synthesis of many Janus structures [17]. On the other hand, as another example, people have theoretically predicted the electronic, vibrational, elastic, and piezoelectric properties of Janus MoTe [18]. These features prove the great potential of Janus MXY in electronic and photoelectric applications.

New 2D materials have been continuously explored, and their physical properties and potential applications have been intensively investigated. Recently, a high quality MoSi₂N₄

monolayer has been successfully fabricated by chemical vapor deposition (CVD) [19], which makes the new 2D material MA_2Z_4 family attract extensive attention, in which $M = Mo, W, V, Nb, Ta, Ti, Zr, Hf,$ or Cr ; $A = Si$ or Ge ; and $Z = N, P,$ or As [20]. At present, people have revealed the physical properties of the MA_2Z_4 monolayer through first principles calculations, such as structural stability, electronic properties, visible absorption coefficient, Rashba spin splitting, carrier mobility, and so on. These findings revealed that the fascinating MA_2Z_4 families are promising 2D materials for many applications due to their outstanding properties [21–25]. Transition metal nitride (TMN) monolayers in this family, such as $MoSi_2N_4$ and $MoGe_2N_4$, are promising candidates for optoelectronic nanodevices [26–29]. Theoretical investigations have been carried out for MA_2Z_4 monolayer and van der Waals heterostructures (vdWH) based on it. Graphene, C_2N , MoS_2 , and $MoSe_2$ have been selected to build vdWH with $MoSi_2N_4$, which paves the way for the design of high-performance photocatalysts and optoelectronic nanodevices in the future [30–33].

vdWH, which is stacked by two or more layered materials, is one of the research hotspots of 2D materials. Compared with 2D monolayer materials, vdWH can improve electrical properties, light absorption efficiency, catalytic hydrogen production performance, etc. [34–36]. Although many vdWHs have been manufactured experimentally or predicted theoretically, research on 2D MA_2Z_4 -based vdWHs is still in its infancy. Here, considering that both Janus $MoSTe$ and $MoGe_2N_4$ monolayers are indirect band gap semiconductors [28,37] and both have good absorption coefficients in the visible region, we combine the advantages of these two monolayers and construct different configurations of $MoSTe/MoGe_2N_4$ vdWHs. The electronic structure, optical properties, and the effects of the biaxial strains and the interlayer distances are investigated. The calculation shows that a $MoSTe/MoGe_2N_4$ vdWH can be a semimetal or a direct band gap semiconductor with different stacking configurations. In addition, the optical absorption of $MoSTe/MoGe_2N_4$ vdWH has been greatly improved both in the visible and ultraviolet regions compared with those of the individual monolayers. There are transitions between semimetal and semiconductor when biaxial strains and interlayer distances are changed in $MoSTe/MoGe_2N_4$ vdWH. In addition, the compression strain enables $MoSTe/MoGe_2N_4$ vdWH to significantly increase the absorption intensity in the visible and ultraviolet regions, while the tensile strain reduces the absorption in the visible region. The construction of the $MoSTe/MoGe_2N_4$ vdWH improves the electronic structure and the optical absorption compared to its individual monolayers, and these properties can also be modulated by the strain and interlayer distance. $MoSTe/MoGe_2N_4$ vdWH can be widely used in optoelectronic nanodevices.

2. Calculation Methods

All our calculations are based on the first principles approach through density functional theory (DFT), which is implemented using the Vienna Ab-initio Simulation Package (VASP) [38,39]. Taking into account the exchange and other correlation energies, the general gradient approximation (GGA) [40] in the form of Perdew–Burke–Ernzerh (PBE) is used. In addition, the DFT-D3 correction method proposed by Grimme is used in the calculations [41]. For the structural optimization, electronic properties, and optical properties, the k-point in the first Brillouin zone is taken as $6 \times 6 \times 1$ according to the Monkhorst–Pack scheme. In order to avoid the influence of interlayer interactions, a vacuum layer of 20 Å is placed perpendicular to the interface in the z-direction. During the calculation, the plane wave cut-off energy is set to 500 eV. At the same time, in order to fully optimize the atomic structure, the convergence accuracy of the force during relaxation is set to less than 0.01 eV/Å for each atom and 10^{-6} eV for the energy convergence of electron self-consistency.

Optical propagation through a medium, and the dielectric function is used to describe the absorption coefficient [42,43]. The formula is as follows:

$$\varepsilon(\omega) = \varepsilon_1(\omega) + i\varepsilon_2(\omega). \quad (1)$$

Dielectric function ϵ is made up of two parts, real part ϵ_1 and imaginary part ϵ_2 . The real part represents the capacity of the material to store energy, and ϵ_1 is given by the Kramers–Kronig formula:

$$\epsilon_1(\omega) = 1 + \frac{2}{\pi} P \int_0^{\infty} \frac{\epsilon_2^{\alpha\beta}(\omega')\omega'}{\omega'^2 - \omega^2 + i\eta} d\omega' \quad (2)$$

where P represents the principal value of the integral.

The imaginary part ϵ_2 represents the loss factor, which is shown in the following equation:

$$\epsilon_2(\omega) = \frac{4\pi^2 e^2}{\Omega} \lim_{q \rightarrow 0} \sum_{c:v:k} 2\omega_k \delta(\epsilon_{ck} - \epsilon_{vk} - \omega) \times \langle u_{ck+e_\alpha q} | u_{vk} \rangle \langle u_{ck+e_\beta q} | u_{vk} \rangle^*. \quad (3)$$

where Ω stands for the volume, α and β are the Cartesian components, e_α and e_β are the unit vectors, v and c represent matrix elements of the transition from the valence band state (u_{vk}) to the conduction band state (u_{ck}), and ϵ_{ck} and ϵ_{vk} denote for the energies of the conduction and the valence band, respectively.

The absorption coefficient $\alpha(\omega)$ is derived from the above two equations:

$$\alpha(\omega) = \frac{\sqrt{2}\omega}{c} \left\{ \left[\epsilon_1^2(\omega) + \epsilon_2^2(\omega) \right]^{\frac{1}{2}} - \epsilon_1(\omega) \right\}^{\frac{1}{2}}. \quad (4)$$

3. Results and Discussions

Before studying the properties of MoSTe/MoGe₂N₄ vdWH, we first investigate the atomic structure and the electronic characteristics of the two monolayers. In Figure S1, both monolayers of Janus MoSTe and MoGe₂N₄ are semiconductors. As shown in Figure S1a, the Janus MoSTe monolayer shows a hexagonal atomic structure with the space group P6m1. The Mo atom is connected to the S and Se atoms on each side by covalent bonds. The optimized lattice parameters are $a = b = 3.362 \text{ \AA}$, the Mo-S bond length is $d_{\text{Mo-S}} = 2.437 \text{ \AA}$, and the Mo-Te bond length is $d_{\text{Mo-Te}} = 2.718 \text{ \AA}$. At the same time, the conduction band minimum (CBM) of the Janus MoSTe monolayer appears at the K point, while the valence band maximum (VBM) appears at the Γ point, and the indirect band gap is 1.027 eV. The results are consistent with previous reports [37]. The projected density of states (PDOS) of the Janus MoSTe monolayer is shown in Figure S1a. The CBM mainly comes from the strong hybridization between Mo-d, Te-p, and S-p orbitals, while the VBM is contributed from Mo-d and S-p orbitals. Similarly, the MoGe₂N₄ monolayer has a hexagonal crystal structure with space group P6m1. Atoms in the MoGe₂N₄ monolayers are connected to each other by covalent bonds in the order of N-Ge-N-Mo-N-Ge-N, so MoGe₂N₄ can be regarded as MoN₂ layers sandwiched between two Ge-N bilayers. The optimized MoGe₂N₄ monolayers have lattice constants of $a = b = 3.037 \text{ \AA}$; the bond length of the Mo-N bond is $d_{\text{Mo-N}} = 2.130 \text{ \AA}$, and it is $d_{\text{Si-N}} = 1.892 \text{ \AA}$ for the Si-N bond. As shown in Figure S1b, the MoGe₂N₄ monolayer is a semiconductor with an indirect band gap of 0.901 eV. Its CBM is located at the K point and is mainly contributed from Mo-d orbitals, while the VBM is located in the K- Γ path in the 2D hexagonal Brillouin zone and mainly comes from strong hybridization between Mo-d, N-p, and Ge-s orbitals. These results are consistent with the previously reported results [22].

MoSTe/MoGe₂N₄ vdWH is constructed by a $\sqrt{3} \times \sqrt{3}$ Janus MoSTe supercell and 2×2 MoGe₂N₄ supercell, and the lattice mismatch value is 1.48% in this case. The stacking modes are named Te_n vdWH when the Te atoms of Janus MoSTe are close to the MoGe₂N₄ layer. Similarly, the stacking method is named S_n vdWH when the S atom of Janus MoSTe is close to the MoGe₂N₄ layer. There are six possible stacking configurations for Te_n and S_n, respectively, so there are twelve different stacking configurations, which are shown in Figure S2. To check the stability of these different stacking configurations, we calculate their

binding energies. The binding energy can be expressed as $E_b = E_{\text{total}} - E_{\text{MoSTe}} - E_{\text{MoGe}_2\text{N}_4}$, where E_{total} , E_{MoSTe} , and $E_{\text{MoGe}_2\text{N}_4}$ are the total energies of the MoSTe/MoGe₂N₄ vdWH, the Janus MoSTe, and the MoGe₂N₄ monolayer, respectively. The binding energies for the twelve stacking configurations are listed in Table S1. All binding energies are negative, which indicates that the twelve stacking configurations are stable. The binding energies of Te₄ and S₄ are lowest compared with the others, which means that these two stacking configurations are the most stable. Therefore, in the subsequent calculations, we focus on Te₄ and S₄, which are shown in Figure 1. We calculate the ab initio molecular dynamics (AIMD) of Te₄ and S₄ at 300 K with a simulation duration of 5 ps and a time step of 1 fs. As shown in Figure 1, it is found that the fluctuation of energies is small, which indicates that the two configurations are stable.

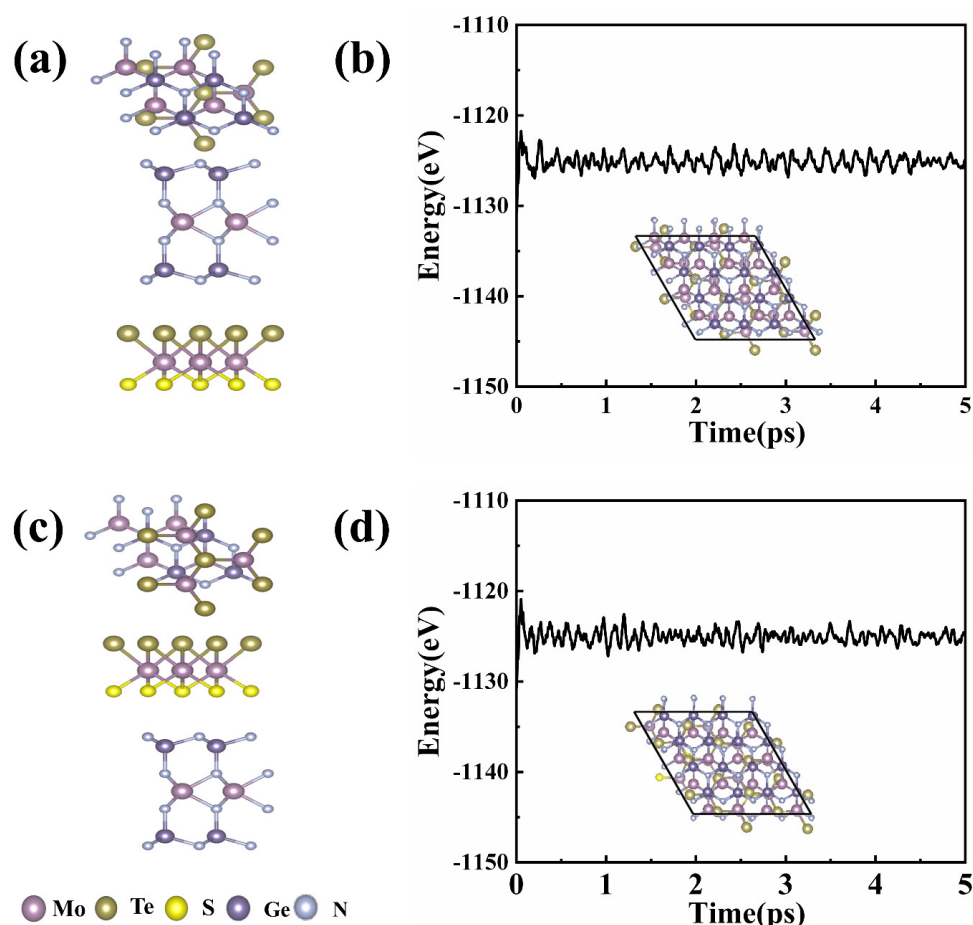


Figure 1. Top and side views of the optimized atomic structures of (a) Te₄-MoSTe/MoGe₂N₄ vdWH and (b) S₄-MoSTe/MoGe₂N₄ vdWH. The AIMD results are shown in (c) Te₄-MoSTe/MoGe₂N₄ vdWH and (d) S₄-MoSTe/MoGe₂N₄ vdWH, and the insets show the crystal structure at the end state.

As shown in Figure 2, based on the orbital characteristics, we plot the energy band structure and the PDOS of the vdWH using different color plots. It can be found that different stacking patterns can produce different electronic structures due to different interlayer coupling effects. Figure 2a shows the Te₄-MoSTe/MoGe₂N₄ stacked conformation. There is no band gap in Te₄-MoSTe/MoGe₂N₄ vdWH. Its CBM is located at point Γ , mainly coming from the contribution of the MoGe₂N₄ monolayer, and VBM is located at point K, mainly coming from the contribution of the Janus MoSTe monolayer. This vdWH has a non-overlapping band gap between the two semiconductors, which is crossed through the vdWH by band-to-band quantum tunneling and charge transfer. Therefore, the Te₄-MoSTe/MoGe₂N₄ vdWH is a semimetal, which can be widely used in the design of various high-speed and low-power devices [44]. It can be seen from PDOS that CBM mainly

comes from N-p orbitals and VBM mainly comes from S-p orbitals. Figure 2b shows the S_4 -MoSTe/MoGe₂N₄ vdWH stacked configuration, and it is clear that S_4 -MoSTe/MoGe₂N₄ vdWH has a direct band gap of 0.27 eV, where both CBM and VBM are located at the Γ point. It can be seen that the CBM and VBM come from the contributions of the Janus MoSTe monolayer and the MoGe₂N₄ monolayer, respectively. It can be seen from the PDOS that the CBM is mainly from the Mo-s orbital and the VBM is mainly from the S-p orbital. This direct band gap semiconductor of S_4 -MoSTe/MoGe₂N₄ vdWH can effectively facilitate the separation of electrons and holes in real space. Therefore, this finding makes MoSTe/MoGe₂N₄ vdWH a promising candidate for the fabrication of high-performance optoelectronic devices with suppressed carrier recombination.

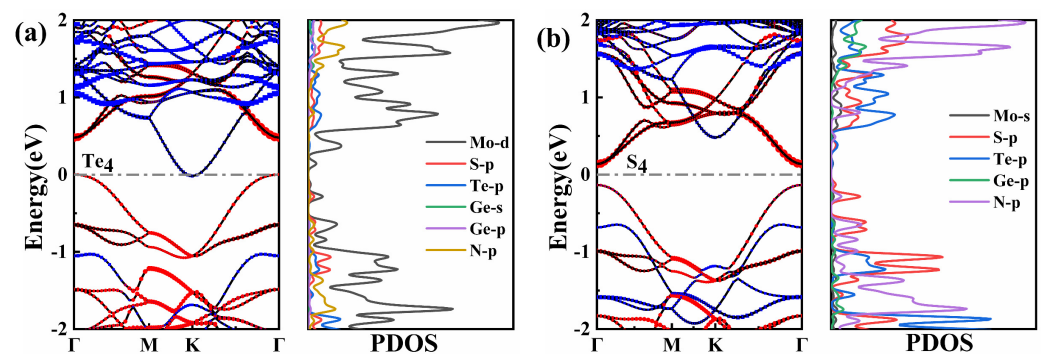


Figure 2. The weighted band structures and PDOS of (a) Te_4 -MoSTe/MoGe₂N₄ vdWH and (b) S_4 -MoSTe/MoGe₂N₄ vdWH. The Fermi levels are set to zero. Red represents the weights by Janus MoSTe; blue indicates weights by MoGe₂N₄.

Figure 3 shows the electrostatic potential and differential charge density for two stacked configurations of MoSTe/MoGe₂N₄ vdWH. The electrostatic potential can reflect the difficulty of the electron transport system and has an impact on the electrical properties of the material. As can be seen from Figure 3, the electrostatic potentials of the two stacking configurations are slightly different. The electrostatic potential of the Janus MoSTe monolayer is deeper than that of the MoGe₂N₄ monolayer. The electrostatic potential of Te_4 -MoSTe/MoGe₂N₄ vdWH decreases by 2.09 eV, while the electrostatic potential of S_4 -MoSTe/MoGe₂N₄ vdWH decreases by 5.05 eV. Therefore, there is a built-in electric field between the two layers with the direction from the Janus MoSTe layer to the MoGe₂N₄ layer, which affects the charge injection and the carrier motion to some extent.

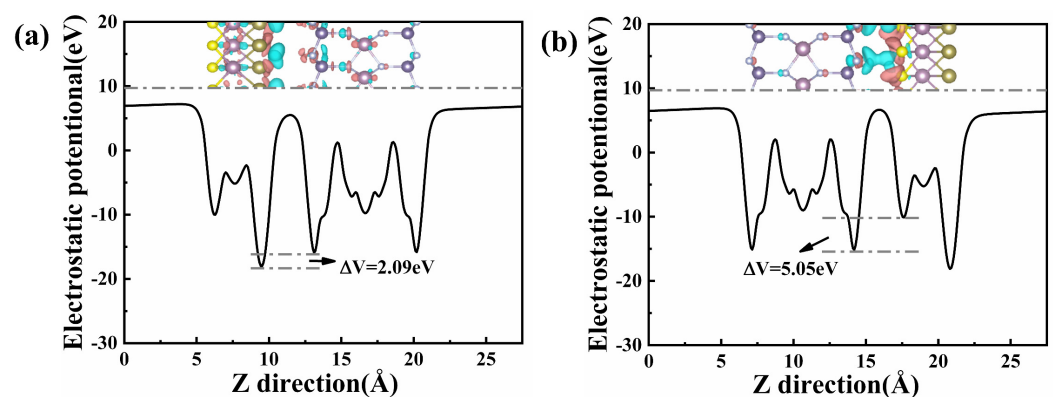


Figure 3. The electrostatic potential diagram in (a) Te_4 -MoSTe/MoGe₂N₄ vdWH and (b) S_4 -MoSTe/MoGe₂N₄ vdWH. The top inset shows the differential charge density. The pink and blue colors indicate electron accumulation and loss, respectively. The isosurface value is $0.0002 \text{ eV } \text{\AA}^{-1}$.

In order to visualize the charge transfer of MoSTe/MoGe₂N₄ vdWH, we calculate the charge density difference as follows:

$$\Delta\rho = \rho_{\text{MoSTe/MoGe}_2\text{N}_4} - \rho_{\text{MoSTe}} - \rho_{\text{MoGe}_2\text{N}_4} \quad (5)$$

where $\rho_{\text{MoSTe/MoGe}_2\text{N}_4}$, ρ_{MoSTe} , and $\rho_{\text{MoGe}_2\text{N}_4}$ denote the charge density of MoSTe/MoGe₂N₄ vdWH, Janus MoSTe, and MoGe₂N₄ monolayer, respectively. In Figure 3, the pink represents electron accumulation and blue represents electron depletion. For Te₄-MoSTe/MoGe₂N₄ vdWH, the electrons are gathered around the Mo atoms in Janus MoSTe and MoGe₂N₄ layers, and there is no electron transfer between the two layers, as shown in Figure 3a. From Figure 3b, we can clearly see the electron distribution between the two monolayers in S₄-MoSTe/MoGe₂N₄ vdWH. We observe that the electron accumulates in the Janus MoSTe layer, while there is an electron depletion in the MoGe₂N₄ layer. This shows that the electron is transferred from the MoGe₂N₄ layer to the Janus MoSTe layer. By Bader charge analysis, we found that only a small amount of 0.575 eV electrons are transferred from the Janus MoSTe layer to the MoGe₂N₄ layer.

Figure 4 shows the calculated optical absorption spectrum of Janus MoSTe, MoGe₂N₄, Te₄-MoSTe/MoGe₂N₄ vdWH, and S₄-MoSTe/MoGe₂N₄ vdWH. In the visible region (1.6 eV < E < 3.1 eV), both the Janus MoSTe monolayer and MoGe₂N₄ monolayer have a high absorption coefficient. Combining the advantages of the two monolayers, the absorption coefficient is significantly increased after the vdWH is formed. Compared with the two independent monolayers, both Te₄-MoSTe/MoGe₂N₄ vdWH and S₄-MoSTe/MoGe₂N₄ vdWH show stronger absorption coefficients. In the ultraviolet (UV) region, the absorption intensity has a maximum. Due to interlayer coupling between Janus MoSTe and MoGe₂N₄ monolayers, the band gap of MoSTe/MoGe₂N₄ vdWH is reduced and charge transfer takes place, resulting in an enhanced absorption spectrum. Thus, MoSTe/MoGe₂N₄ vdWH has a higher optical response and is more favorable for applications in optoelectronic devices compared with monolayers.

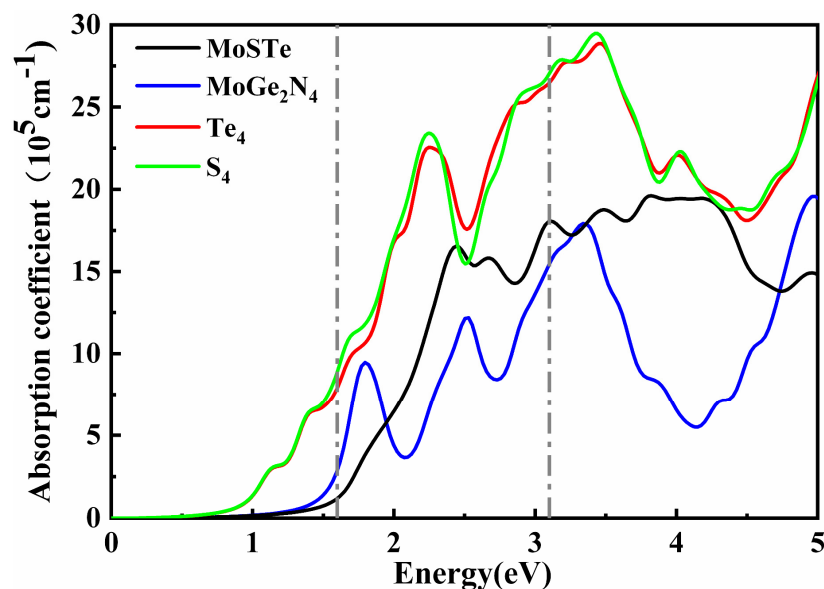


Figure 4. Optical absorption spectrum of Janus MoSTe, MoGe₂N₄, Te₄-MoSTe/MoGe₂N₄ vdWH, and S₄-MoSTe/MoGe₂N₄ vdWH.

Thus far, researchers have found that by applying external stress, it is possible not only to change the electronic properties of two-dimensional materials but also to achieve modulation of the absorption coefficient. In the following study, biaxial strains are applied to Te₄-MoSTe/MoGe₂N₄ vdWH and S₄-MoSTe/MoGe₂N₄ vdWH, and both their electronic and optical properties are investigated. The equations for calculating the strain

magnitude of the materials are as follows [45]: $\varepsilon = [(a - a_0)/a_0] \times 100\%$, where a and a_0 represent the lattice constants for applied and unapplied stress, respectively. $\varepsilon < 0$ means compressive stress, and $\varepsilon > 0$ means tensile stress. Stress of $-5\% \leq \varepsilon \leq 5\%$ is applied to Te_4 -MoSTe/MoGe₂N₄ vdWH and S_4 -MoSTe/MoGe₂N₄ vdWH, respectively. The variation of band gap with biaxial strain for the Janus MoSTe monolayer, MoGe₂N₄ monolayer, and MoSTe/MoGe₂N₄ vdWH is shown in Figure 5.

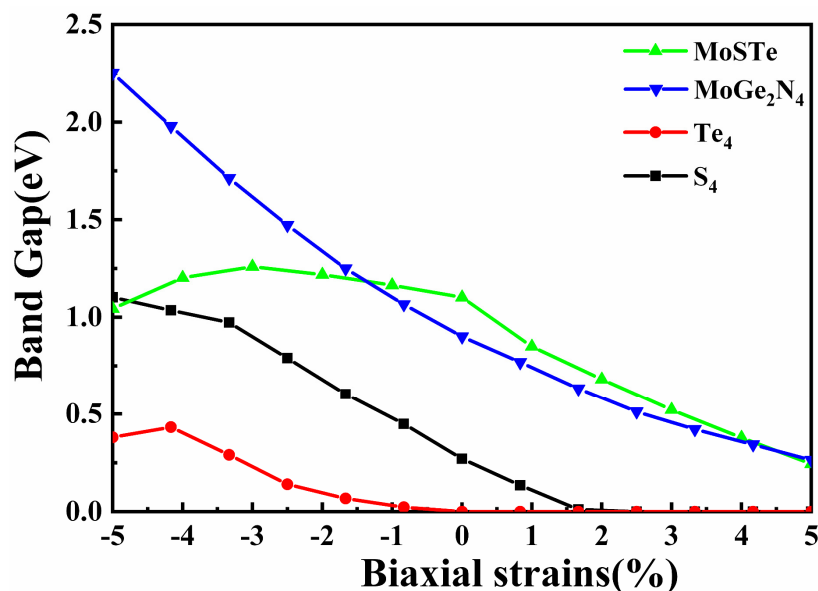


Figure 5. Effect of applied biaxial strain on band gap for Janus MoSTe, MoGe₂N₄, Te_4 -MoSTe/MoGe₂N₄ vdWH, and S_4 -MoSTe/MoGe₂N₄ vdWH, respectively.

The formed MoSTe/MoGe₂N₄ vdWH has a significantly smaller band gap compared with those of the Janus MoSTe and the MoGe₂N₄ monolayer. Te_4 -MoSTe/MoGe₂N₄ vdWH still shows metallicity, and there is no band gap when tensile strain is applied. However, with increasing compressive strain, the band gap of Te_4 -MoSTe/MoGe₂N₄ vdWH gradually increases from zero, and the electronic structure changes from semimetal to semiconductor. When the compressive strain is greater than -5% , the band gap starts to decrease again. At this time, its CBM and VBM are coming from the MoGe₂N₄ monolayer and Janus MoSTe monolayer, respectively, as shown in Figure S3. The band gap of S_4 -MoSTe/MoGe₂N₄ vdWH increases with increasing compressive strain and decreases with increasing tensile strain. However, when a biaxial strain larger than $+2\%$ is applied, there is no band gap and S_4 -MoSTe/MoGe₂N₄ vdWH becomes a semimetal. Therefore, the electronic structure of MoSTe/MoGe₂N₄ vdWH can be regulated to change between semimetal and semiconductor by applying biaxial strain.

The optical properties of MoSTe/MoGe₂N₄ vdWH also change after the biaxial strain is applied. As shown in Figure 6, we investigate the variation patterns of the absorption coefficients of Te_4 -MoSTe/MoGe₂N₄ vdWH and S_4 -MoSTe/MoGe₂N₄ vdWH with biaxial strain. It is found that the effects of biaxial strain on the absorption intensity of the two vdWHs are basically the same pattern. When compressive strain is applied, the absorption coefficient of MoSTe/MoGe₂N₄ vdWH decreased with increasing compressive intensity and increased with increasing tensile intensity in the infrared region. In the visible and UV regions, the absorption coefficient of MoSTe/MoGe₂N₄ vdWH increases with increasing compressive strength and decreases with increasing tensile strength. It can be seen that compressive strain increases the absorption coefficient of MoSTe/MoGe₂N₄ vdWH in the visible and UV regions, while tensile strain increases the absorption coefficient of the vdWH in the infrared region. Therefore, biaxial strain can also effectively manipulate the absorption properties of MoSTe/MoGe₂N₄ vdWH.

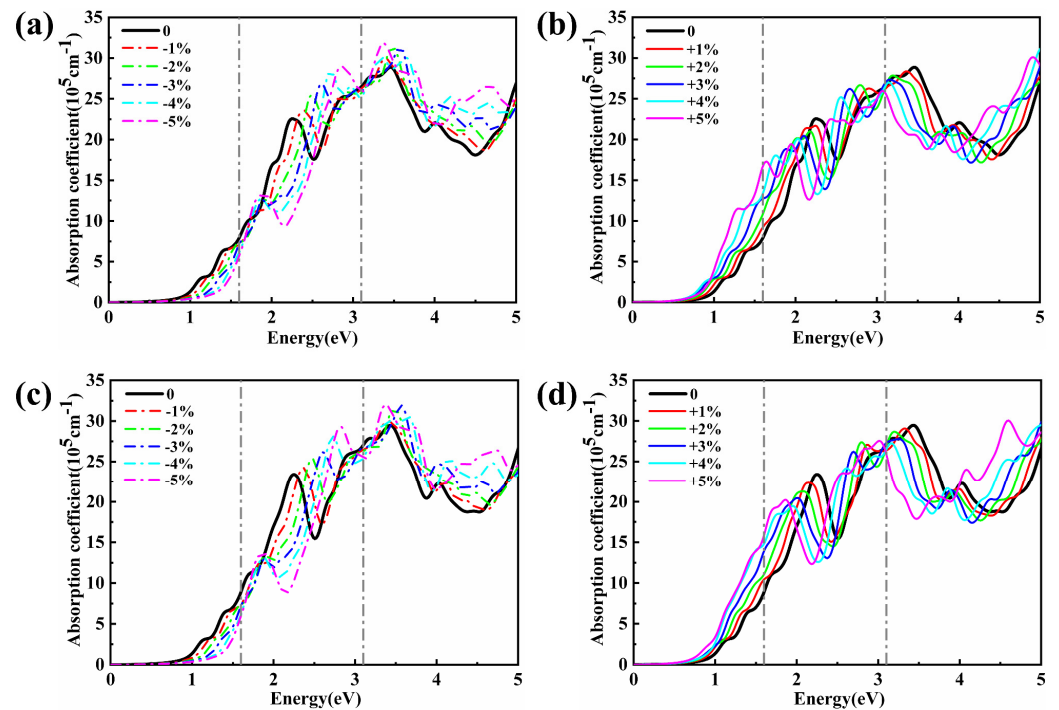


Figure 6. Optical absorption spectrum of (a,b) $\text{Te}_4\text{-MoSTe/MoGe}_2\text{N}_4$ vdWH and (c,d) $\text{S}_4\text{-MoSTe/MoGe}_2\text{N}_4$ vdWH under biaxial strain. Negative and positive values represent compressive stress and tensile stress, respectively.

The variations of the band gaps with different interlayer distances for $\text{Te}_4\text{-MoSTe/MoGe}_2\text{N}_4$ and $\text{S}_4\text{-MoSTe/MoGe}_2\text{N}_4$ vdWH are shown in Figure 7, where the equilibrium interlayer distances are 3.4 Å and 3.1 Å, respectively. We find that there is no band gap in $\text{Te}_4\text{-MoSTe/MoGe}_2\text{N}_4$ vdWH when the interlayer distance is less than 3.63 Å. When the interlayer distance is larger than 3.63 Å, the band gap of $\text{Te}_4\text{-MoSTe/MoGe}_2\text{N}_4$ vdWH increases with an increase in the interlayer distance. The $\text{Te}_4\text{-MoSTe/MoGe}_2\text{N}_4$ vdWH changes between semimetal and indirect band gap semiconductors when the interlayer distance changes. The weight band structures of $\text{Te}_4\text{-MoSTe/MoGe}_2\text{N}_4$ and $\text{S}_4\text{-MoSTe/MoGe}_2\text{N}_4$ vdWH at different interlayer distances are depicted in Figure S4. We find that the band gap in $\text{S}_4\text{-MoSTe/MoGe}_2\text{N}_4$ vdWH increases with an increasing interlayer distance and decreases with a decreasing interlayer distance. When the interlayer distance is less than 2.3 Å, the band gap of the $\text{S}_4\text{-MoSTe/MoGe}_2\text{N}_4$ vdWH becomes small and close to zero. The results indicate that changing the interlayer distance can also regulate the electronic structure of the $\text{MoSTe/MoGe}_2\text{N}_4$ vdWH.

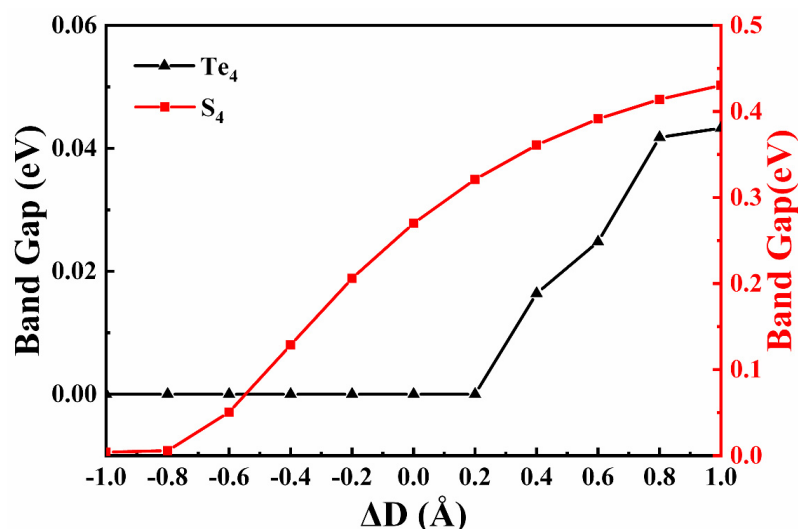


Figure 7. Variations in band gaps of the Te₄-MoSTe/MoGe₂N₄ vdWH and S₄-MoSTe/MoGe₂N₄ vdWH with the change in interlayer distances. Black and red correspond to Te₄-MoSTe/MoGe₂N₄ vdWH and S₄-MoSTe/MoGe₂N₄ vdWH, respectively.

4. Conclusions

In conclusion, we systematically researched the atomic structure, electronic properties, and optical properties of MoSTe/MoGe₂N₄ vdWH using the VASP software package based on density functional theory. Two monolayers of Janus MoSTe and MoGe₂N₄ are stacked into heterostructures by van der Waals forces. The thermodynamic stability of MoSTe/MoGe₂N₄ vdWH is examined using AIMD simulations. Two stacking modes have low binding energies, i.e., Te₄-MoSTe/MoGe₂N₄ vdWH and S₄-MoSTe/MoGe₂N₄ vdWH. Compared with the two separate monolayers, the band gap of MoSTe/MoGe₂N₄ vdWH is reduced and the light absorption intensity is significantly increased. The energy band structure of MoSTe/MoGe₂N₄ vdWH can be manipulated by applying a biaxial strain, and the transition between semimetal and semiconductor appears when the biaxial strain changes from -5% to $+5\%$. At the same time, the applied strain can also modulate the light absorption intensity. In the visible and UV regions, the absorption coefficient increases with increasing compressive strain and decreases with increasing tensile strain. In addition, different interlayer distances contribute to a change in the band gap, and a shift between semiconductor and semimetal can be realized. In other words, the electronic and optical properties of MoSTe/MoGe₂N₄ vdWH can be manipulated by external conditions, such as applying external strain and changing the interlayer distances. Our research has shown that MoSTe/MoGe₂N₄ vdWH is a potential candidate for high-performance optoelectronic nanodevices.

Supplementary Materials: The following are available online at <https://www.mdpi.com/article/10.3390/nano11123338/s1>, Figure S1: Band structures and PDOS of (a) Janus MoSTe monolayer and (b) MoGe₂N₄ monolayer. The Fermi levels are set to zero, Figure S2: The optimized top and side views of MoSTe/MoGe₂N₄ vdWH for twelve different stacking patterns, Figure S3: Band structures of (a) (b) Te₄-MoSTe/MoGe₂N₄ vdWH and (c) (d) S₄-MoSTe/MoGe₂N₄ vdWH under biaxial strain. Red and blue represent the weights from Janus MoSTe and MoGe₂N₄ monolayers, respectively. Negative and positive values mean compressive stress and tensile stress, Figure S4: Band structures of (a) (b) Te₄-MoSTe/MoGe₂N₄ vdWH and (c) (d) S₄-MoSTe/MoGe₂N₄ vdWH under different interlayer distances, where the equilibrium interlayer distances are 3.4 Å and 3.1 Å, respectively. Red and blue represent the weights from Janus MoSTe and MoGe₂N₄ monolayers, respectively, Table S1: Binding energies (E_b) of the optimized MoSTe/MoGe₂N₄ vdWH for the twelve different stacking patterns.

Author Contributions: Writing—original draft preparation, J.W.; writing—review and editing, X.Z.; formal analysis, G.H.; supervision, J.R.; project administration, X.Y. All authors have read and agreed to the published version of the manuscript.

Funding: This research was funded by the National Natural Science Foundation of China, grant Nos. 11674197 and 11974215 and the Natural Science Foundation of Shandong Province, grant No. ZR2021MA105.

Data Availability Statement: The data are available on request from the corresponding author.

Conflicts of Interest: The authors declare no conflict of interest.

References

1. Yuan, S.; Pang, S.-Y.; Hao, J. 2D transition metal dichalcogenides, carbides, nitrides, and their applications in supercapacitors and electrocatalytic hydrogen evolution reaction. *Appl. Phys. Rev.* **2020**, *7*, 021304. [[CrossRef](#)]
2. Zavabeti, A.; Jannat, A.; Zhong, L.; Haidry, A.A.; Yao, Z.; Ou, J.Z. Two-Dimensional Materials in Large-Areas: Synthesis, Properties and Applications. *Nano-Micro Lett.* **2020**, *12*, 66. [[CrossRef](#)] [[PubMed](#)]
3. Chaves, A.; Azadani, J.G.; Alsalman, H.; da Costa, D.R.; Frisenda, R.; Chaves, A.J.; Song, S.H.; Kim, Y.D.; He, D.; Zhou, J.; et al. Bandgap engineering of two-dimensional semiconductor materials. *npj 2D Mater. Appl.* **2020**, *4*, 28. [[CrossRef](#)]
4. Khan, K.; Tareen, A.K.; Aslam, M.; Wang, R.; Zhang, Y.; Mahmood, A.; Ouyang, Z.; Zhang, H.; Guo, Z. Recent developments in emerging two-dimensional materials and their applications. *J. Mater. Chem. C* **2020**, *8*, 387–440. [[CrossRef](#)]
5. Kumar, R.; Sahoo, S.; Joanni, E.; Singh, R.K.; Yadav, R.M.; Verma, R.K.; Singh, D.P.; Tan, W.K.; del Pino, A.P.; Moshkalev, S.A.; et al. A review on synthesis of graphene, h-BN and MoS₂ for energy storage applications: Recent progress and perspectives. *Nano Res.* **2019**, *12*, 2655–2694. [[CrossRef](#)]
6. Carvalho, A.; Ribeiro, R.M.; Neto, A.H.C. Band nesting and the optical response of two-dimensional semiconducting transition metal dichalcogenides. *Phys. Rev. B* **2013**, *88*, 115205. [[CrossRef](#)]
7. Ruppert, C.; Aslan, O.B.; Heinz, T.F. Optical Properties and Band Gap of Single- and Few-Layer MoTe₂ Crystals. *Nano Lett.* **2014**, *14*, 6231–6236. [[CrossRef](#)] [[PubMed](#)]
8. Tedstone, A.A.; Lewis, D.J.; O'Brien, P. Synthesis, Properties, and Applications of Transition Metal-Doped Layered Transition Metal Dichalcogenides. *Chem. Mater.* **2016**, *28*, 1965–1974. [[CrossRef](#)]
9. Qiu, B.; Zhao, X.W.; Hu, G.C.; Yue, W.W.; Yuan, X.B.; Ren, J.F. Tuning optical properties of Graphene/WSe₂ heterostructure by introducing vacancy: First principles calculations. *Phys. E Low Dimens. Syst. Nanostruct.* **2020**, *116*, 113729. [[CrossRef](#)]
10. Li, R.; Li, L.-J.; Cheng, Y.; Huang, W. Recent Advances in van der Waals Heterojunctions Based on Semiconducting Transition Metal Dichalcogenides. *Adv. Electron. Mater.* **2018**, *4*, 1800270. [[CrossRef](#)]
11. Xia, C.; Xiong, W.; Du, J.; Wang, T.; Peng, Y.; Li, J. Universality of electronic characteristics and photocatalyst applications in the two-dimensional Janus transition metal dichalcogenides. *Phys. Rev. B* **2018**, *98*, 165424. [[CrossRef](#)]
12. Zhang, X.; Lai, Z.; Ma, Q.; Zhang, H. Novel structured transition metal dichalcogenide nanosheets. *Chem. Soc. Rev.* **2018**, *47*, 3301–3338. [[CrossRef](#)] [[PubMed](#)]
13. Dong, L.; Lou, J.; Shenoy, V.B. Large In-Plane and Vertical Piezoelectricity in Janus Transition Metal Dichalcogenides. *ACS Nano* **2017**, *11*, 8242–8248. [[CrossRef](#)]
14. Zhao, X.; Liu, F.; Ren, J.; Qu, F. Valleytronic and magneto-optical properties of Janus and conventional TiBrI/CrI₃ and TiX₂/CrI₃ (X = Br, I) heterostructures. *Phys. Rev. B* **2021**, *104*, 085119. [[CrossRef](#)]
15. Chen, J.; Wu, K.; Ma, H.; Hu, W.; Yang, J. Tunable Rashba spin splitting in Janus transition-metal dichalcogenide monolayers via charge doping. *RSC Adv.* **2020**, *10*, 6388–6394. [[CrossRef](#)]
16. Yao, Q.-F.; Cai, J.; Tong, W.-Y.; Gong, S.-J.; Wang, J.-Q.; Wan, X.; Duan, C.-G.; Chu, J.H. Manipulation of the large Rashba spin splitting in polar two-dimensional transition-metal dichalcogenides. *Phys. Rev. B* **2017**, *95*, 165401. [[CrossRef](#)]
17. Lai, X.; Zhang, Y.; Zheng, Y.; Xiang, X.; Ye, H.; Liu, W.; Liu, Y. Catalytic activity for hydrogen evolution reaction in square phase Janus MoSSe monolayer: A first-principles study. *Phys. Low Dimens. Syst. Nanostruct.* **2021**, *126*, 114485. [[CrossRef](#)]
18. Yagmurcukardes, M.; Sevik, C.; Peeters, F.M. Electronic, vibrational, elastic, and piezoelectric properties of monolayer Janus MoSTe phases: A first-principles study. *Phys. Rev. B* **2019**, *100*, 045415. [[CrossRef](#)]
19. Hong, Y.-L.; Liu, Z.; Wang, L.; Zhou, T.; Ma, W.; Xu, C.; Feng, S.; Chen, L.; Chen, M.-L.; Sun, D.-M.; et al. Chemical vapor deposition of layered two-dimensional MoSi₂N₄ materials. *Science* **2020**, *369*, 670–674. [[CrossRef](#)] [[PubMed](#)]
20. Novoselov, K.S. Discovery of 2D van der Waals layered MoSi₂N₄ family. *Natl. Sci. Rev.* **2020**, *7*, 1842–1844. [[CrossRef](#)]
21. Chen, J.; Tang, Q. The Versatile Electronic, Magnetic and Photo-Electro Catalytic Activity of a New 2D MA₂Z₄ Family**. *Chem. Eur. J.* **2021**, *27*, 9925–9933. [[CrossRef](#)]
22. Mortazavi, B.; Javvaji, B.; Shojaei, F.; Rabczuk, T.; Shapeev, A.V.; Zhuang, X. Exceptional piezoelectricity, high thermal conductivity and stiffness and promising photocatalysis in two-dimensional MoSi₂N₄ family confirmed by first-principles. *Nano Energy* **2021**, *82*, 105716. [[CrossRef](#)]
23. Wang, L.; Shi, Y.; Liu, M.; Zhang, A.; Hong, Y.-L.; Li, R.; Gao, Q.; Chen, M.; Ren, W.; Cheng, H.-M.; et al. Intercalated architecture of MA₂Z₄ family layered van der Waals materials with emerging topological, magnetic and superconducting properties. *Nat. Commun.* **2021**, *12*, 1–10. [[CrossRef](#)]
24. Yang, J.-S.; Zhao, L.; Li, S.-Q.; Liu, H.; Wang, L.; Chen, M.; Gao, J.; Zhao, J. Accurate electronic properties and non-linear optical response of two-dimensional MA₂Z₄. *Nanoscale* **2021**, *13*, 5479–5488. [[CrossRef](#)] [[PubMed](#)]

25. Zhong, H.; Xiong, W.; Lv, P.; Yu, J.; Yuan, S. Strain-induced semiconductor to metal transition in MA_2Z_4 bilayers ($M = Ti, Cr, Mo$; $A = Si$; $Z = N, P$). *Phys. Rev. B* **2021**, *103*, 085124. [[CrossRef](#)]
26. Bafekry, A.; Faraji, M.; Hoat, D.M.; Shahrokhi, M.; Fadlallah, M.M.; Shojaei, F.; Feghhi, S.A.H.; Ghergherehchi, M.; Gogova, D. $MoSi_2N_4$ single-layer: A novel two-dimensional material with outstanding mechanical, thermal, electronic and optical properties. *J. Phys. D Appl. Phys.* **2021**, *54*, 155303. [[CrossRef](#)]
27. Yao, H.; Zhang, C.; Wang, Q.; Li, J.; Yu, Y.; Xu, F.; Wang, B.; Wei, Y. Novel Two-Dimensional Layered $MoSi_2Z_4$ ($Z = P, As$): New Promising Optoelectronic Materials. *Nanomaterials* **2021**, *11*, 559. [[CrossRef](#)]
28. Nguyen, C.; Hoang, N.V.; Phuc, H.V.; Sin, A.Y.; Nguyen, C.V. Two-Dimensional Boron Phosphide/ $MoGe_2N_4$ van der Waals Heterostructure: A Promising Tunable Optoelectronic Material. *J. Phys. Chem. Lett.* **2021**, *12*, 5076–5084. [[CrossRef](#)]
29. Pham, D.K. Electronic properties of a two-dimensional van der Waals $MoGe_2N_4/MoSi_2N_4$ heterobilayer: Effect of the insertion of a graphene layer and interlayer coupling. *RSC Adv.* **2021**, *11*, 28659–28666. [[CrossRef](#)]
30. Bafekry, A.; Faraji, M.; Ziabari, A.A.; Fadlallah, M.M.; Nguyen, C.V.; Ghergherehchi, M.; Feghhi, S.A.H. A van der Waals heterostructure of $MoS_2/MoSi_2N_4$: A first-principles study. *New J. Chem.* **2021**, *45*, 8291–8296. [[CrossRef](#)]
31. Cai, X.; Zhang, Z.; Zhu, Y.; Lin, L.; Yu, W.; Wang, Q.; Yang, X.; Jia, X.; Jia, Y. A two-dimensional $MoSe_2/MoSi_2N_4$ van der Waals heterostructure with high carrier mobility and diversified regulation of its electronic properties. *J. Mater. Chem. C* **2021**, *9*, 10073–10083. [[CrossRef](#)]
32. Pham, K.D.; Nguyen, C.Q.; Nguyen, C.V.; Cuong, P.V.; Hieu, N.V. Two-dimensional van der Waals graphene/transition metal nitride heterostructures as promising high-performance nanodevices. *New J. Chem.* **2021**, *45*, 5509–5516. [[CrossRef](#)]
33. Zeng, J.; Xu, L.; Yang, Y.; Luo, X.; Li, H.-J.; Xiong, S.X.; Wang, L.-L. Boosting the photocatalytic hydrogen evolution performance of monolayer C₂N coupled with $MoSi_2N_4$: Density-functional theory calculations. *Phys. Chem. Chem. Phys.* **2021**, *23*, 8318–8325. [[CrossRef](#)] [[PubMed](#)]
34. Liang, S.-J.; Cheng, B.; Cui, X.; Miao, F. Van der Waals Heterostructures for High-Performance Device Applications: Challenges and Opportunities. *Adv. Mater.* **2020**, *32*, 1903800. [[CrossRef](#)]
35. Guo, J.; Zhao, X.; Hu, G.; Ren, J.; Yuan, X. Observation and manipulation of valley polarization in two-dimensional $H-Tl_2O/CrI_3$ heterostructure. *Appl. Surf. Sci.* **2021**, *558*, 149604. [[CrossRef](#)]
36. Guo, Y.; Wang, J.; Hu, G.; Yuan, X.; Ren, J. Strain-tunable electronic and optical properties of novel $MoSSe/InSe$ van der Waals heterostructures. *Phys. Lett. A* **2021**, *404*, 127395. [[CrossRef](#)]
37. Idrees, M.; Din, H.U.; Ali, R.; Rehman, G.; Hussain, T.; Nguyen, C.V.; Ahmad, I.; Amin, B. Optoelectronic and solar cell applications of Janus monolayers and their van der Waals heterostructures. *Phys. Chem. Chem. Phys.* **2019**, *21*, 18612–18621. [[CrossRef](#)]
38. Bučko, T.; Lebègue, S.; Hafner, J.; Ángyán, J.G. Tkatchenko-Scheffler van der Waals correction method with and without self-consistent screening applied to solids. *Phys. Rev. B* **2013**, *87*, 064110. [[CrossRef](#)]
39. Grimme, S.; Ehrlich, S.; Goerigk, L. Effect of the Damping Function in Dispersion Corrected Density Functional Theory. *J. Comput. Chem.* **2011**, *32*, 1456–1465. [[CrossRef](#)]
40. Perdew, J.P.; Burke, K.; Ernzerhof, M. Comment on “Generalized gradient approximation made simple”—Reply. *Phys. Rev. Lett.* **1998**, *80*, 891. [[CrossRef](#)]
41. Grimme, S.; Antony, J.; Ehrlich, S.; Krieg, H. A consistent and accurate ab initio parametrization of density functional dispersion correction (DFT-D) for the 94 elements H-Pu. *J. Chem. Phys.* **2010**, *132*, 154104. [[CrossRef](#)] [[PubMed](#)]
42. Gajdoš, M.; Hummer, K.; Kresse, G.; Furthmüller, J.; Bechstedt, F. Linear optical properties in the projector-augmented wave methodology. *Phys. Rev. B* **2006**, *73*, 045112. [[CrossRef](#)]
43. Eberlein, T.; Bangert, U.; Nair, R.R.; Jones, R.; Gass, M.; Bleloch, A.L.; Novoselov, K.S.; Geim, A.; Briddon, P.R. Plasmon spectroscopy of free-standing graphene films. *Phys. Rev. B* **2008**, *77*, 233406. [[CrossRef](#)]
44. Özçelik, V.O.; Azadani, J.G.; Yang, C.; Koester, S.J.; Low, T. Band alignment of two-dimensional semiconductors for designing heterostructures with momentum space matching. *Phys. Rev. B* **2016**, *94*, 035125. [[CrossRef](#)]
45. Zubko, P.; Catalan, G.; Tagantsev, A.K. Flexoelectric Effect in Solids. *Annu. Rev. Mater. Res.* **2013**, *43*, 387–421. [[CrossRef](#)]